

# AN OFF-LINE SCAN OF THE BATSE DAILY RECORDS AND A LARGE UNIFORM SAMPLE OF GAMMA-RAY BURSTS

BORIS E. STERN,<sup>1,2,3</sup> YANA TIKHOMIROVA,<sup>2,3</sup> DMITRII KOMPANEETS,<sup>2</sup> ROLAND SVENSSON,<sup>3</sup> AND JURI POUTANEN<sup>3</sup>

*Draft version December 24, 2018*

## ABSTRACT

During a scan of the archival BATSE daily records covering the entire 9.1 years (TJD 8369 - 11690) of the BATSE operation, 3923 gamma-ray bursts (GRBs) have been detected. 2074 of these GRBs are previously known BATSE triggers while 1849 of them are new non-triggered bursts. It is important that all events were detected in the same type of data and were processed with the same procedure. Therefore these 3923 GRBs constitute a uniform sample. We describe the procedures of the data reduction, the selection of the GRB candidates, and the statistical tests for possible non-GRB contaminations. We also describe the test burst method and the information obtained using the test bursts. We have created a publically available electronic data base<sup>4</sup> containing this sample.

*Subject headings:* gamma-rays: bursts – methods: data analysis

## 1. INTRODUCTION

The sample of gamma-ray bursts (GRBs) detected by the Burst and Transient Source Experiment (BATSE) (Fishman et al. 1989) on the *Compton Gamma-Ray Observatory (CGRO)* is a few times larger than the yield of all other experiments that have detected GRBs. Despite that the breakthrough in 1997 concerning the distance to GRBs was associated with the precise localization of a small number of GRBs by *Bepo-SAX*, the value of the large BATSE sample cannot be overestimated. Problems where a large statistics of GRBs as well as the wide brightness range of the BATSE sample are crucial are, e.g.,

1. estimating the total rate of GRBs in the Universe,
2. searching for different subclasses of GRBs,
3. observing gravitational lensing of GRBs,
4. searching for repetition of GRBs,
5. estimating the intrinsic luminosity function of GRBs.

The list can be made longer. Here, we mention only those problems which are directly associated with the goals of this work.

Nevertheless, the BATSE sample (i.e., the sample of the triggered events included in the BATSE catalogs) is smaller than what it could be at the actual sensitivity of BATSE. The reason for this is a difficult variable background. The trigger threshold must be higher and the trigger integration time must be shorter than for the case of a constant background. Otherwise a high rate of triggers would have caused severe problems in the data acquisition. The BATSE trigger adjusted to the background

conditions missed many weak but still highly significant GRBs. Some bursts were also missed due to other reasons (data readouts, etc.).

Many of these non-triggered GRBs can be confidently identified in the BATSE daily records which cover the whole period of the *CGRO* operation. Off-line searches for non-triggered bursts with less rigid off-line trigger criteria can substantially increase the sensitivity of BATSE and extend the sample of GRBs both in number and in brightness range.

The first sample of non-triggered GRBs was found by Rubin et al. (1992). A systematic search for non-triggered GRBs in 6 years of *CGRO* BATSE data was performed by Kromers et al. (1997, 1998,<sup>5</sup> 2000, hereafter K97, K98, K00). Schmidt (1999) performed a scan of the BATSE daily records for  $\sim$ 6 years (TJD 8365 - 10528) using a triggering procedure close to the BATSE trigger and found about 400 bursts missed by BATSE itself.

The main feature of our off-line scan of the BATSE data is the measurement of the efficiency of the GRB detection as a function of brightness using artificial test bursts (e.g., Stern et al. 2000b). This method plays the role of being a calibration of the experiment. Using the measured efficiency function, we found that the  $\log N - \log P$  distribution of GRBs does not bend down near the BATSE threshold but continues almost without curvature down to a peak brightness of  $0.1 \text{ ph s}^{-1} \text{ cm}^{-2}$ .

In this paper, we concentrate on a description of the data reduction and the tests for possible non-GRB contaminations. We also describe the publically available data base containing our sample of GRBs. Earlier preliminary versions of this data base and some first results were briefly reported in Stern et al. (1999a, 1999b, 2000a, 2000b).

<sup>1</sup>Institute for Nuclear Research, Russian Academy of Sciences, Moscow 117312, Russia

<sup>2</sup>Astro Space Center of Lebedev Physical Institute, Profsoyuznaya 84/32, Moscow 117810, Russia (stern@lukash.asc.rssi.ru, jana@anubis.asc.rssi.ru, dkompan@dpc.asc.rssi.ru)

<sup>3</sup>Stockholm Observatory, SE-133 36 Saltsjöbaden, Sweden (stern, jana, svensson, juri@astro.su.se)

<sup>4</sup>[http://www.astro.su.se/groups/head/grb\\_archive.html](http://www.astro.su.se/groups/head/grb_archive.html)

<sup>5</sup>The catalog is available at <http://space.mit.edu/BATSE/>

In §§2 - 5, we describe the procedures of the scan, the identification of GRBs, and the GRB data reduction. In §6, we describe the general characteristics of our GRB sample, compare the sample with the Kommers et al. and the BATSE catalogs, and describe the data archive containing the sample. Section 7 is devoted to various statistical tests for possible non-GRB contaminations using hardness ratios, angular and latitude distributions. We obtain upper limits to the contaminations caused by terrestrial phenomena, solar flares, and Galactic X-ray objects. In §8, we estimate the efficiency of the scan and present the final  $\log N - \log P$  distribution, which considerably differs from those of the BATSE and the Kommers et al. catalogs. The implication is the existence of many more weak GRBs.

## 2. THE DATA SCAN

We used the 1024 ms time resolution BATSE data (DIS-CLA) from the ftp archive at the Goddard Space Flight Center.<sup>6</sup> The main array of the raw data consists of the number counts in the 8 BATSE Large Area Detectors (LADs) in the 4 energy channels with 1.024 s time resolution for the whole period of observations (excluding some data gaps).

Examples of data fragments are presented in Figure 1. The data are difficult to process because of the large diversity of interfering phenomena: the variable background, the flaring and noising ionosphere, solar flares, noising astrophysical sources, and occultations of sources by the Earth causing steps in the count rate curves. In addition, the situation is confused by numerous data gaps.

The complicated background makes usual statistical estimates of the detection efficiency useless. The estimate derived considering only Poisson fluctuations does not work when non-Poisson variability of the background is strong. Then there are a variety of reasons for missing a detectable burst: a data gap, interference with a variable source, or high ionospheric activity. The corresponding probabilities are in all cases brightness dependent. In this case, a realistic estimate of the detection efficiency should be based on some kind of simulation of the real detection conditions using real data. Such a simulation was implemented in the form of a test burst method (Stern et al. 2000b).

Artificial test bursts were prepared from a sample of 500 real triggered BATSE bursts of durations longer than 1 s and were added to the original “daily” count rate records. Each test burst was created by sampling one of the 500 bursts with a random number and rescaling its amplitude to a randomly sampled expected peak count rate with a proper Poisson noise. The distribution of peak count rates prescribed to the test bursts is shown in Figure 2. Originally we expected that our detection threshold would be at  $0.08 \text{ counts s}^{-1} \text{ cm}^{-2}$ . Then we improved the efficiency of the search and found that we detect many events below this threshold. We then reduced the lower limit to  $0.06 \text{ counts s}^{-1} \text{ cm}^{-2}$ . However, this still seems not be sufficiently small.

The procedure of the scan is described in Stern et al. (1999b, 2000b). Briefly, it consists of adding test bursts to the data (see above), the triggering, an express-analysis, the identification, and the classification.

The off-line trigger consists of three criteria to be satisfied simultaneously. The first is a traditional one: a significant rise in the counts over the estimated background. For the brightest detector, a  $4\sigma$  excess was required, and for the second brightest, a  $2.5\sigma$  excess. This is lower than the BATSE threshold and similar to that of K98. The excess was checked for in time intervals (i.e., triggering time scales) of 1 bin (1.024 s), 2 bins, 4 bins, and 8 bins. The longer triggering integration time scales gives the main gain in the sensitivity as compared to BATSE. The second criterion is a sufficiently high variability around the trigger time. The variability is expressed as the residual  $\chi^2$  after making a linear fit of the signal. This  $\chi^2$  should exceed a threshold value. The third criterion is a check whether the signal can be attributed to Cyg X-1. The signal was fitted by the photon flux from the Cyg X-1 direction and the residual was checked for a sufficient variability as in the previous case.

The two latter criteria, which were not used previously, turned out to be very efficient in eliminating false triggers reducing their number by more than an order of magnitude.

Each trigger was followed by a preliminary estimate of whether the trigger is a GRB candidate (the person performing the scan was unaware of whether the candidate event was a real or a test burst). Most triggers were rejected by a visual analysis. Usually false triggers were caused by occultation steps, sharp variations of the ionospheric background, or solar flares. The selection criteria used in this step are similar to those described in §4, they are just softer, and the count rate was just assumed to be proportional to the detector projection area in the burst direction ( $\propto \cos \theta$ ). For all selected events, we recorded fragments of the original data and some preliminary estimates of their parameters.

At the next step, we identified which recorded events were test bursts or BATSE triggers. Finally, we processed all recorded events and made a more careful selection of GRBs using the procedures described in §3 and §4.

The rate of our off-line detections of GRBs depends on time (see Figure 3). It reflects the quality of the data, the intensity of noise-generating sources (Cyg X-1, X-ray novae), and the solar activity. One can see a gradual increase in the number of detected GRBs with time. It results from improvements in the software and from the experience gained during the scan. Note that our rate of observing non-triggered GRBs is well correlated with that of K98.

## 3. THE FITTING OF THE GRB LOCATION AND PHOTON FLUX

The aim of the fit is to find the best burst location, spectrum, and intensity describing the count rate data in 8 detectors and 4 energy channels. This is done using the detector response matrix, hereafter DRM,  $D_{ljk}$ , where  $l$  is the photon energy index,  $k$  is the channel number, and  $j$  is the detector number.  $D_{ljk}$  depends on the burst location, the satellite orientation, and the location of the Earth with respect to the *CGRO* coordinate system. To calculate the DRM we used a version of the code written by G. Pendleton which was used for the localization of the

<sup>6</sup>Available at: <http://cossc.gsfc.nasa.gov/pub/data/batse/daily/>

BATSE triggered bursts (Pendleton et al. 1999, hereafter P99). The localization procedure itself differs from that implemented in the LOCBURST code by P99 in some details as described below.

As a spectral hypothesis, we used the Band parametrization (Band et al. 1993), which consists of 4 parameters: the low energy power law slope,  $\alpha$ ; the high energy power law slope,  $\beta$ ; the transition (peak) energy,  $E_0$ ; and the normalization factor. The problem is that we have only 4 experimental values: the counts in the 4 energy channels. Therefore a straightforward fit using the Band function would be degenerate.

We solved this problem using a sample of Band parametrizations (Band et al. 1993) of real time-integrated spectra of 54 GRBs. At the first step, we determined which of the 54 spectra (i.e., which combination of  $\alpha$ ,  $\beta$  and  $E_0$ ) that provides the best fit of the time-integrated brightest part of the burst using a pre-estimated burst location. Then we made a spectral fit for each time bin of the burst varying the two spectral parameters,  $E_0$  and the normalization factor keeping  $\alpha$  and  $\beta$  fixed. Such a fit is statistically meaningful and our chosen model describing the GRB spectral evolution as a variation of  $E_0$  seems natural.

The location fit used by P99 assumed that the GRB spectra are power laws (i.e., a 2-parameter description), but this is a worse description of real GRB spectra as compared to the Band function.

For a given spectrum  $F_l$  we have

$$C_{ijk} = \sum_l D_{ljk} F_l I_i / F_{50-300} = d_{jk} I_i, \quad (1)$$

where  $C_{ijk}$  is the net GRB signal in counts in the  $i$ -th time bin, the  $j$ -th detector, and the  $k$ -th energy channel, and  $F_{50-300}$  is the integral of the incident photon number spectrum in the 50 - 300 keV energy range. In this normalization,  $I_i$  is the photon flux in units of  $\text{ph s}^{-1} \text{cm}^{-2}$ .

The value to be minimized is

$$\chi^2 = \sum_{ijk} \frac{(d_{jk} I_i + B_{ijk} - S_{ijk})^2}{S_{ijk}}, \quad (2)$$

where  $B_{ijk}$  is the estimated background for time bin  $i$ , and  $S_{ijk}$  is the total measured counts. The parameters free to vary are: 2 parameters for the whole event to describe the burst location (the factor  $d_{jk}$  depends on location); 1 parameter for the choice of the spectrum from the Band sample; and 2 parameters for each time bin for photon flux  $I_i$  and the spectral peak energy  $E_0$ . The background is estimated as a linear function of time, independently for each detector and each energy channel using two fitting windows, one before and one after the main peak of the event. These windows were set manually using a visual interpretation of the count rate profile. In some rare difficult cases, only one background fitting window was used.

The value of  $\chi^2$  was calculated for a few thousand locations over a wide area of the sky. Using the  $\chi^2$  map of the sky, we defined the best fit location, the  $1\sigma$  error boundary, and the quality of the event as a GRB candidate (see §4). The most serious problem in the location fit is the poor accuracy of the DRM for the detectors which do not see the burst directly but still detect the burst due to photon scattering by the Earth's atmosphere or due

to penetration through the satellite. A precise calculation of the DRM is an extremely difficult problem as one should take into account the 3D mass distribution of the *CGRO*. In the LOCBURST algorithm, the final localization fit is performed only for the 4 or 6 brightest detectors. This reduces the systematic error for the best fit location. However, this option causes a problem when we make the localization for a weak burst where a wide  $\chi^2$  map of the sky is needed (see §4). For different locations, different detectors become the brightest and it is not easy to find the 4 or 6 brightest detectors from the data.

As far as our main interest concerns weak events which requires a large area  $\chi^2$  map, we preferred to use the fit for all 8 detectors. Another advantage of the 8 detector fit is a slightly better signal to noise ratio for the fitting net signal given by equation (1).

The systematic errors of our procedure is probably slightly worse than that of LOCBURST. However, the difference is considerable only for very bright bursts. A more exact localization could be achieved in the next iteration using a refined DRM and reducing the number of detectors participating in the fit. However, the exact localization of strong bursts is beyond the scope of this work at its present stage. For deviations between our and the BATSE locations, see §6.

The best fit value of the photon flux,  $I_i$ , for a given burst location and photon spectrum is:

$$I_i = \frac{\sum_{jk} (S_{ijk} - B_{ijk}) d_{jk} / S_{ijk}}{\sum_{jk} d_{jk}^2 / S_{ijk}}. \quad (3)$$

The fitting count rate (that we prefer to use instead of the photon flux,  $I_i$ , for estimating the peak brightness) is then defined by equation (1), or, in units of  $\text{counts s}^{-1} \text{cm}^{-2}$  as

$$c_{ik} = \sum_m (d_{mk} / s_m) I_i, \quad (4)$$

where  $m$  is the index of the detector having the largest projected area  $s_m$  in the burst direction.

The quantities used in this paper to represent the time profiles and the brightness of GRBs are:

1. The count rate in the 50 - 300 keV energy band and the  $i$ -th time bin:  $c_i = c_{i2} + c_{i3}$ , counts  $\text{s}^{-1} \text{cm}^{-2}$ , with  $c_{i2}$  and  $c_{i3}$  given by equation (4).
2. The peak count rate:  $c$ , counts  $\text{s}^{-1} \text{cm}^{-2}$ , which is a function of  $c_i$ , see §5.2.
3. The net (fitting) count rate:  $C_{ik} = \sum_j C_{ijk}$ , counts  $\text{s}^{-1}$ , where  $j$  is the detector number, see equation (1), or the net count rate in the 50 - 300 keV energy band:  $C_i = C_{i2} + C_{i3}$ .
4. The peak photon flux:  $I$ , which is a function of  $I_i$ , see §5.2.

#### 4. THE IDENTIFICATION OF GRBS

The main quantitative criterion for selecting real events associated with astrophysical sources from the variations of the terrestrial background or other fluctuations was based on the residual  $\chi^2$  map of the sky. The same criterion was used as the significance threshold. Calculating

the residual  $\chi^2$  as a function of the burst location (eq. 2) we define the “ $1\sigma$  area”, i.e., a region where  $\chi^2 - \chi_0^2 < \sqrt{2N}$  where  $N$  is the number of the degrees of freedom, and  $\chi_0^2$  is the minimum value of  $\chi^2$ . The location error according to our preference is the maximum distance,  $\delta_1$ , from the best fit location to the boundary of the  $1\sigma$  area. Similarly, we define the  $4\sigma$  region and the maximum distance,  $\delta_4$ , from the best fit location. Our criterion which any event without any exception should pass to be considered as a GRB candidate is  $\delta_4 < 90^\circ$ . Note, that  $4\sigma$  is the excess of the residual  $\chi^2$  for the fit at a  $90^\circ$  displacement. The *statistical significance* of an event (defined by the  $\chi^2$  with respect to the background) is always above  $7\sigma$  when the  $\delta_4$  criterion is satisfied.

This criterion is optional, of course. It was chosen empirically achieving a good agreement between the results of applying it and the visual recognition of a burst-like event. The  $\delta_4$  criterion efficiently sorts out the fluctuations of the diffuse ionospheric background. Examples of events which have  $\delta_4$  close to its threshold value are shown in Figure 4.

Further criteria were more qualitative and subjective. First, we checked whether one of the variable sources (the Sun, Cyg X-1, or one of the known X-ray transients currently active) was inside or close to the  $1\sigma$  area. Then we applied additional requirements: a large hardness, especially for the case of the Sun; and a large domination over the typical current fluctuations of the source in the cases of Cyg X-1 and X-ray transients (a large domination over both Poisson and non-Poisson noise was a general requirement).

Short soft events were treated as outbursts of X-ray pulsars. The location of such events was always consistent with the location of one of the known X-ray pulsars.

For each event we checked visually the signal in different detectors with the requirement that the signal is visible in more than one detector. However, no requirements for the significance of the signal in the second brightest detector were applied - the signal should just be visually recognized.

Special attention was paid to the “context” of the event: a GRB should be well isolated in order to be accepted. If we saw a persistent noise from approximately the same direction and of comparable intensity, or a high ionospheric activity, we discarded the event. The isolation criterion is a subjective one to some extent as it is very difficult to formalize.

There were no “good” events with a localization significantly below the Earth’s horizon. Such event were only marginally significant or did not satisfy the  $\delta_4$ -criterion. Therefore there was no reason to use the location relative to the Earth’s horizon as an independent criterion. Nevertheless events located near the horizon were treated more suspiciously if the ionospheric activity was high.

## 5. ESTIMATING THE PEAK BRIGHTNESS OF GRBS

### 5.1. The Choice of the Measure for the GRB Brightness

There are two natural choices for the measure of the strength of GRBs. One is a time integral of the GRB signal: the photon fluence, the energy fluence, or the total counts. Another option is to use the peak characteristics: the peak photon flux, the peak energy flux, or the peak count rate. If we try to estimate the GRB distance distribution, a measure which is closer to a standard candle (i.e.,

that has a smaller intrinsic dispersion) would be preferable. We do not know this - probably both the fluence and the peak flux have very large dispersions.

The choice is, however, natural as the peak characteristics are much easier to measure. Besides, the detection efficiency depends on the peak count rate rather than on the time-integrated signal. Among the peak characteristics we choose the peak count rate as a measure of the GRB brightness for the following reasons:

- The peak count rate unlike the peak photon flux and energy flux does not depend on the the assumed photon spectra which could be rather uncertain. It is defined by direct measurements.

- The detection efficiency is a direct function of the peak count rate but not of the peak photon flux.

The next issue is the definition of the peak count rate when we have 8 detectors with different orientations. The best choice at this step is the *fitting count rate*,  $C_{ik}$  or its reduced value  $c_{ik}$  (see §3), i.e., the best fit hypothesis of the true signal.

### 5.2. The Estimate of the Peak Count Rate

The weakest GRBs we deal with have a peak count rate of the same order of magnitude as the Poisson fluctuations at 1.024 s time resolution. Therefore, if we define the peak count rate as the content of the brightest time bin, we probably just choose the highest Poisson fluctuation and thus overestimate the brightness, perhaps by a factor 2 or more for the weakest events. If we smooth the signal, e.g. by averaging over several time bins, we reduce the Poisson noise but then we may loose true short peaks of the GRB signal. A compromise between smoothing and preserving the time resolution is the two iteration schemes described in Stern, Poutanen & Svensson (1999).

In the first iteration, we find the shortest time scale,  $\Delta T_j = 2^j \times 1.024$  s,  $j = 0, 1, 2, 3$ , on which the signal has a significant variation between neighboring time bins (using a  $4.3\sigma$  threshold). Then we search for the  $\Delta T_j$ -interval where the count rate is the largest. (If  $\Delta T = 1.024$  s, the search is completed.)

If  $j > 0$ , we make a second iteration searching for a significant excess in a fraction  $\delta T_l$  of the brightest  $\Delta T_j$ -interval ( $l < j$ ). The significance threshold,  $h_l$ , depends on the time scale  $2^l \times 1024$  s at this step. The values of  $h_l$  were optimized empirically comparing prescribed (expected) and measured count rates for test bursts and were set to  $h_0 = 3.5\sigma$ ,  $h_1 = 2.4\sigma$ ,  $h_3 = 1.4\sigma$ .

The result of this method is shown in Figure 6. One can see that a reasonable linearity between the expected and the measured count rates has been achieved. Nevertheless, after getting rid of the Poisson bias we still have a smaller bias of a similar origin. Events enhanced by positive Poisson fluctuations have a higher probability to be detected. Therefore we observe some systematic excess of the measured amplitude over the expected one for the weakest bursts where the detection efficiency is low. This bias is accounted for by the efficiency matrix (see §8).

As far as we use different units for the peak brightness, it would be useful to give the approximate ratio between the peak count rate and the peak photon flux. This ratio versus the peak count rate is shown in Figure 7. There is no evident correlation between the ratio and the brightness.

The relation between peak count rate and peak brightness can be expressed as  $c = 0.7504I \pm 0.063$ , where the rms variance is given as the error.

## 6. THE SAMPLE AND THE DATA ARCHIVE

We performed the scan of DISCLA data for the full 9.1 years of BATSE observations up to the *CGRO* deorbiting (TJD 8369 - 11690). The number of events in our sample classified as GRBs is 3923, 1849 of them are non-triggered, and 2074 we identified with BATSE triggers.

The peak count rate distributions of these GRBs are shown in Figure 8. Note that some non-triggered events are very strong (the strongest one has a peak flux of 24 photons  $\text{s}^{-1} \text{cm}^{-2}$ ). The reason for BATSE not detecting some strong bursts is the dead time when the trigger was disabled during data readouts or when *CGRO* passed through regions of very high ionospheric activity.

Durations of GRBs were estimated using  $T_{90}$  (Kouveliotou et al. 1993), i.e., as the time interval between the emission of 5% and 95% of the total burst photon fluence. The measurement of  $T_{90}$  has considerable uncertainties when applied to weak bursts. The result depends on the time intervals (windows) where the signal and the background are measured and therefore depends on the subjective impressions of the researcher estimating what is the signal and what are the fluctuations of the background.

The duration distribution for our sample is shown in Figure 9. One can see that non-triggered bursts are slightly shorter on average. This can be explained by the brightness dependent bias: by losses of some episodes of weak bursts. The relation between our and the BATSE estimates of  $T_{90}$  is shown in Figure 10. Large deviations probably result from the uncertainties mentioned above. Our estimates of  $T_{90}$  for short events are strongly biased due to the 1.024 s resolution and the Poisson fluctuations. There is a large probability that an event with  $T_{90} < 1$  s will be distributed in two time bins and therefore will be estimated as 2 s long, or will merge with a nearby Poisson fluctuation.

The distribution of the best fit locations of the GRBs in our sample over the sky is shown in Figure 11. No significant deviations from the BATSE exposure function (see Paciesas et al., 1999, and Figure 17) have been found.

### 6.1. Comparison with the BATSE and Krommers et al. Catalogs

During the period of our scan BATSE triggered 2704 GRBs. Therefore we missed 635 of the BATSE triggered GRBs. We estimated at a previous stage of the scan (Stern et al. 2000b) that  $\sim 70\%$  of these GRBs were lost due to gaps in the DISCLA data,  $\sim 20\%$  were too short to be detected at 1.024 s resolution, and  $\sim 10\%$  were missed due to various human mistakes.

K98 scanned the time interval TJD 8600 - 10800 and found 873 non-triggered GRBs. We found 1132 non-triggered bursts during that time interval. 745 of them are in the catalog of K98.

Krommers (1999, private communication) and K00 inspected the 387 of our non-triggered events that K98 missed. Krommers confirmed 224 of these events as probable GRBs. 24 of the events were classified by Krommers

as particle precipitations, and 7 as noise. 90 of our events were not classified as the off-line trigger of K98 missed those events due to nearby data gaps. 31 events were classified by K98 as “unknown” for their softness (i.e., a very weak or no significant signal in energy channel 3).

We checked most of the 128 events that are in the K98 catalog but that are missing in our sample. We confirm 90 of them as GRBs, 13 we classify as particle precipitations, 4 as long delayed precursors of triggered GRBs, and 2 as solar flares. 12 of these 128 events were missed by our trigger.

We do not include the 90 GRBs of K98 confirmed by us into our sample as the efficiency we estimate does not account for such additional events.

The comparison of our estimates of the peak fluxes of GRBs in the 50 - 300 keV range with those of K98 and BATSE is shown in Figure 12. One can see a reasonable agreement except for a few events where the disagreement could result from errors in the setting of the fitting windows. This could, e.g., cause that a part of an event could be confused with the background. In general, the agreement between our and the BATSE estimates is better than between our and those of K98 in the medium brightness range where a meaningful comparison can be made.

The deviations between our best locations and those from the K98 and the BATSE catalogs are shown in Figure 13. Most of the deviations are within the  $1\sigma$  errors. There is, however, a substantial tail to much larger deviations caused by systematic errors. Very large deviations can result from the choice of different local minima in the location fit. The peak in the distribution of the deviations between our and the BATSE locations is between 2 and 2.5 degrees for bright GRBs. This value approximately characterizes our typical systematic error for the locations. The average systematic error of LOCBURST as estimated by P99 is  $\sim 1.7$  degrees. Our procedure is not optimized for precise localization of strong bursts, since we do not take into account nonlinear effects occurring at very high count rates and do not turn off less illuminated detectors in the fit as LOCBURST does. Our scheme is adjusted for convenient and reliable fits of weak bursts.

There is an additional source of systematic errors which can be substantial for weak GRBs: the uncertainties in the interpolation of the background. This bias is difficult to estimate. It can be responsible for large (more than  $1\sigma$ ) deviations for weak events.

### 6.2. Bursts near the Detection Threshold

The weakest events of the sample have peak fluxes below 0.1 ph  $\text{s}^{-1} \text{cm}^{-2}$ . They have been detected due to their long duration using the 4 or 8 second trigger time scales. They are not necessarily the least significant events. One can get a feeling of the weakest part of our sample from Figure 14 and Table 1, where we present information on the 11 weakest events detected in the scan and classified as GRBs. The events in Figure 14 and Table 1 are marked by their names consisting of the TJD when the event was detected and an identifying letter. All are more than 20 s long (shorter events are not significant at these brightnesses), are significant, and have good  $\chi^2$  maps. The detection efficiency in this brightness range is  $\sim 0.05$ .

### 6.3. The Data Archive

All data for our GRB sample are electronically available (Stern & Tikhomirova 1999).<sup>7</sup> The archive contains the following data:

1. Tables with names, arrival times, locations, peak brightnesses using different definitions, hardness ratios, and durations ( $T_{90}$ ). BATSE trigger numbers are given for triggered events. Events identified with the GRBs of the K98 catalog are marked.
2. Fragments of raw DISCLA data in FITS format covering the events. The typical time interval covered by the fragments is 300 seconds for shorter ( $< 100$  s) events. For longer events the time interval is extended.
3. Time profiles as the sum of the count rates in the two brightest detectors and in energy channels # 2 and # 3 (the 50 - 300 keV band) in ASCII format. This is the simplest and the most compact representation for the time profiles.
4. Time profiles of GRBs as the fitting count rate,  $C_{ik}$ , with subtracted background, see §3 and §5.1, for the four LAD energy channels in ASCII format. This representation has a better signal/noise ratio than the sum of the count rates in any combination of detectors.
5. All distributions presented in this paper in both graphical and numerical form.

### 7. TESTS FOR NON-GRB CONTAMINATIONS

All our tests for non-GRB contaminations were performed on the sample of 3678 events detected up to TJD 11499 (8.6 years of observations).

#### 7.1. Possible Types of the Contamination

We can divide the possible non-GRB contaminations of the sample into the following categories:

##### 1. Poisson or non-Poisson background fluctuations

The least significant GRBs of our sample are too significant to be reproduced by pure Poisson fluctuations. There are however significant variations of the background due to ionospheric phenomena, occultations of astrophysical sources, and noise generating sources. Such events usually give a bad  $\chi^2$  map (see §4) or do not pass the "isolation" criterion. Nevertheless, we should admit the existence of some cases where a fluctuation may pass all tests. This kind of fluctuations is almost time-symmetric. Therefore we can test for such a kind of contamination by searching for "negative bursts" in sign-inverted count rate data. We performed such tests for 200 days of data records taken in different intervals over a few years representing various background conditions. The rate of triggers was practically the same as in the normal scan. However, only 2 events passed the objective criteria described in §4 (mainly they were rejected by the  $\delta_4$  criterion). Both events are within the "2  $\sigma$  area" of Cyg X-1 and both are not enough isolated, so they should be rejected subjectively. Thus

we constrain the contamination of sign-symmetric background fluctuations to be less than  $\sim 0.5\%$  of the events.

##### 2. Ionospheric events such as particle precipitation

Particle precipitation is a frequent phenomenon taking place at high latitudes: the satellite flies through a cloud of energetic particles emitting bremsstrahlung. Then a more or less time-symmetric hump of counts is recorded in all or most of the detectors. Such events are easily recognizable by comparable signals in detectors facing opposite directions and, correspondingly, by a bad  $\chi^2$  map and residuals. If the precipitation is at some distance from the satellite path, the time profiles in different detectors do not match and again we obtain a bad location fit. The most dangerous events are distant ionospheric flares with fast (shorter than hundred seconds) variability. We observed such events recognizing them by "context", i.e., they occur at a high general ionospheric activity at high latitudes and appear in long series.

##### 3. Solar flares and known variable X-ray sources including X-ray transients and X-ray pulsars.

Surprisingly, solar flares are not a considerable source of the contamination as they are much softer than GRBs. There is some small overlap in hardness. For this reason, we reject some events which could be soft GRBs if they are consistent in location with the Sun. With known X-ray sources we mean those for which we performed a special check.

##### 4. Unknown astrophysical sources emitting bursts similar to GRBs.

These could be other Galactic accreting black holes, hard bursts of other X-ray pulsars, or unknown phenomena (i.e., huge stellar flares). We cannot discriminate such events individually if they overlap with GRBs in their characteristics. We can only sense such contaminations statistically. Such a statistical analysis is presented below.

### 7.2. Hardness Ratios

GRBs are on average harder than any other kind of events that can mimic a GRB. We plot several examples of non-GRB events of known origin together with GRBs in a hardness - brightness diagram, Figure 15, where the hardness ratio is that between the counts in the 50 - 300 and the 20 - 50 energy bands. Outbursts of Cyg X-1 have an almost constant hardness ratio. It is slightly smaller than the average ratio for GRBs. Ionospheric flares have a wider dispersion and partly overlap with GRBs in their hardness ratios, while being softer on average. Bursts of X-ray pulsars are on average considerably softer than GRBs. However, their hardness distribution overlaps with that of GRBs and some hard well-isolated pulses could be included into the sample as GRBs. Large (like tens of events) contamination of this kind would be revealed in the angular distributions of GRBs. The softest events we deal with are solar flares. Their overlap with GRBs in hardness is very small as seen in Figure 15.

If the weakest part of our sample were considerably contaminated with some non-GRB events, we could observe this in the hardness distribution of weak events (this is hardly so for Cyg X-1 which has almost the same hardness ratio as weak GRBs). However, the hardness ratios

<sup>7</sup>The archive is available at: [http://www.astro.su.se/groups/head/grb\\_archive.html](http://www.astro.su.se/groups/head/grb_archive.html)

for the weakest events smoothly extend the hardness vs. brightness correlation of brighter GRBs as seen in Figures 15 and 16. Thus the statistics of the hardness ratios for the weakest bursts does not demonstrate any indications of a considerable contamination.

### 7.3. Angular Distributions

Each kind of non-GRB events has its specific non-isotropic angular distribution which can affect the angular distribution of events of the sample if the latter is contaminated with non-GRBs. Here we analyze several angular distributions of events in the sample. Each of them is sensitive to some kind of non-GRB contamination. Since the weakest part of the sample is more likely to be contaminated, we analyze some angular distributions using the subsample of the weakest GRBs. The polar angular distributions for both real and test bursts are consistent with the BATSE exposure function (see Figure 17).

The distribution of GRBs relative to the Earth's horizon is shown in Figure 18. The shape of the distribution is reasonable: an isotropic distribution above the horizon and a clear step at the horizon. There is no excess of events towards the horizon which could appear if the sample contains many misidentified events of terrestrial (ionospheric) origin.

No excess of events towards the Sun has been found. Figure 19 demonstrates a very wide separation between solar flares and GRBs in a plot of hardness ratio vs angular distance from Sun. One can conclude from Figure 19 that the contamination of the sample by solar flares is negligible.

The distribution of weak GRBs and weak test bursts ( $P < 0.2 \text{ ph s}^{-1} \text{ cm}^{-2}$ ) relative to the direction to Cyg X-1 is shown in Figure 20. There is an evident deficit of both test and real bursts in the direction to Cyg X-1. This is natural as we missed many weak bursts in that direction when subtracting the signal from Cyg X-1. The depression is slightly deeper in the case of test bursts. The corresponding expected number of real bursts in the two last bins (a cone of half opening angle  $26^\circ$  around Cyg X-1) is 11, while the real number is 15. The difference is not significant, of course. The formal  $1\sigma$  confidence interval for contamination by Cyg X-1 is  $4 \pm 5$  events. Brighter outbursts of Cyg X-1 are very rare.

Contaminating X-ray pulsars and variable x-ray sources would give an excess of weak bursts in the direction of the Galactic center. Actually there is, on the contrary, a deficit of both real and test weak bursts in the direction of the Galactic Center. A small fraction of this deficit is explained by the coverage function. A stronger effect appears as a result of worse background conditions in that direction, mainly due to Cyg X-1 ( $\sim 60^\circ$  from the Galactic Center direction).

The formal  $1\sigma$  confidence interval for a Galactic Center subpopulation in our sample for a cone of  $37^\circ$  half opening angle in the direction of the Galactic Center (where both of the X-ray pulsars shown in Figure 15 are located) is  $-10 \pm 10$  events. Similarly we do not see any excess of weak events towards the galactic plane.

### 7.4. Dependence on the Satellite Latitude

The intensity of ionospheric activity strongly depends on the satellite latitude. Particularly, the frequency of particle precipitations sharply increases at high latitudes. Therefore the distribution of the satellite latitude, when an event of our sample was recorded, is sensitive to the contamination of the sample by the ionospheric events. Then we would have an excess of events detected at large Northern and Southern latitudes. The distribution of events along the satellite path should not be uniform as the background conditions are substantially worse at a high latitude. As far as we have common conditions for the detection of real and test bursts, an excess of real events relative to the test bursts can be estimated. Figure 21 shows the results of such a test for all and for the weakest events. There is no excess of real events relative to the test bursts at high latitudes. An approximate  $1\sigma$  upper limit for the contamination of the sample by events of ionospheric origin at latitudes above  $\pm 20^\circ$  (where more than 90% of the particle precipitation events occur, see Fig. 21) is 42 events (i.e., 1.1%) for the full sample and 17 events taking into account only the weakest part of the sample where a misclassification is more probable (at  $P < 0.2 \text{ ph s}^{-1} \text{ cm}^{-2}$ , the 680 weakest GRBs).

### 7.5. Test Summary

Summarizing the results of the tests:

1. The contamination of the sample by solar flares is negligible.
2. The Cyg X-1 contribution is estimated as  $4 \pm 5$  events.
3. The contribution of all sources concentrated within  $37^\circ$  around the Galactic Center direction is constrained to be  $-10 \pm 10$  events.
4. The least constrained source of contamination is produced by ionospheric phenomena because the corresponding angular distributions are the least determined. However, even in this case the contamination is constrained to be at the level of  $\sim 1\%$ .

We should admit the existence of some non-GRB isotropic background of events of a different nature but looking like GRBs. Then this is rather an issue of the classification of GRBs, which is beyond the scope of this paper.

## 8. THE LOG N – LOG P DISTRIBUTION

### 8.1. The Efficiency Function and the Efficiency Matrix

The efficiency function of the search defined as the ratio of the number of detected test bursts to the number of test bursts applied to the data versus the *expected* peak count rate is shown in Figure 22. The result of a direct correction of the measured peak count rate distribution using this efficiency is shown in Figure 23. Such a correction (if we assume that the measured and the expected count rates are identical) is valid for reconstruction of the  $\log N - \log P$  distribution only at a peak brightness that sufficiently exceeds the threshold. Here, the errors in the peak count rates are moderate and symmetric (see Figure 6) and the efficiency changes smoothly. Near the threshold we have to take into account the matrix of the probabilities

of detecting a burst of a given expected count rate with a given measured count rate. Unfortunately, our statistics of the weakest test bursts is too poor because we have underestimated the sensitivity of the scan and cut the distribution of test bursts at a too high expected count rate. One can get a feeling for the situation from Table 2 where we present part of the efficiency matrix. We can see the asymmetry of the matrix near the threshold which results from the selection bias discussed in §5.2.

The matrix is insufficient to perform the exact reconstruction of  $\log N - \log P$  near the threshold. However, we can try to approximate the existing matrix by a reasonable parametrization and to use its extrapolation to smaller count rates. We approximate the efficiency matrix with a factorized expression where the efficiency function, the peak brightness error, and the selection bias were fitted independently:

$$F(c_e, c_m) = 0.70(1 - \exp[-(c_e/c_{e,o})^2])^\nu \times \frac{1}{\sigma\sqrt{\pi}} \exp[\log^2(c_m/c_{m,o})/2\sigma^2], \quad (5)$$

where  $c_e$  is the expected, and  $c_m$  the measured count rate. The first factor is a fit to the efficiency function (Figure 22) with two parameters:  $c_{e,o} = 0.097$  counts  $\text{s}^{-1} \text{cm}^{-2}$  and  $\nu = 2.34$ . The second log-normal factor describes the relative error of the measured count rate:  $\sigma = 0.09(0.08/c_e)^{1/2}$ , and the selection bias is crudely expressed as  $c_{m,o} = c_e + 6.0 \exp(-c_e/6)$ .

## 8.2. The $\log N - \log P$ Distribution

The  $\log N - \log P$  curve for our whole sample of detected events straightforwardly corrected using the efficiency function is shown in Figure 23. Our whole sample is not homogeneous because it contains short events where the peak flux estimate in 1 s time resolution is wrong. To eliminate the corresponding bias we excluded from the distribution all events consisting of one bin (i.e., where only one 1.024 s bin is above 0.5 of the peak flux value). The corresponding efficiency function was calculated using only those test bursts that produce events satisfying the above criterion. Then we have a more or less homogeneous estimate of the peak count rates. The  $\log N - \log P$  distribution of only long events is more relevant for cosmological fits.

As was mentioned above the correction using the efficiency function is not exact especially near the threshold. One should deconvolve the observed peak brightness distribution (Figure 8) using the efficiency matrix. This is easier to do with a forward folding method, i.e., fitting the observed distribution using a convolution of a hypothetical  $\log N - \log P$  distribution with the efficiency matrix. We cannot use “data points” like those in Figure 23 for the hypothetical  $\log N - \log P$  distribution as the forward folding in this case allows large fluctuations between neighboring “data points” and the result is unstable. We should use some smooth function as a hypothesis for the  $\log N -$

$\log P$  distribution but such a fit is beyond the scope of the present paper.

## 9. CONCLUSIONS

With a careful off-line scan of the daily archival data, BATSE becomes a more sensitive instrument with better known characteristics. The detection threshold changes by a factor 2, from  $\sim 0.2 \text{ ph s}^{-1} \text{ cm}^{-2}$  to  $\sim 0.1 \text{ ph s}^{-1} \text{ cm}^{-2}$ . The total number of detected GRBs increases by a factor of 1.7. If we consider only long events (short GRBs could be a different phenomenon), the gain is a factor of  $\sim 2$ . The recognition of the weakest GRBs is still confident and the contamination with events originating from trivial kinds of non-GRBs is small.

As a first result, we see the  $\log N - \log P$  distribution extending down to lower brightnesses almost straight without any indication of a turn-over. This result differs from previous interpretations of the data, which implied that the  $\log N - \log P$  distribution smoothly bends down at low brightness (see the data points of K00 in Figure 23).

One simple consequence is that the estimate of the number of GRBs in the visible Universe should be increased. Just the “visible” part of the  $\log N - \log P$  distribution implies 1200 - 1300 GRBs occurring per year at peak fluxes exceeding  $0.1 \text{ ph s}^{-1} \text{ cm}^{-2}$  (previous versions of the  $\log N - \log P$  distribution implied  $\sim 600$  GRBs per year above  $0.18 \text{ ph s}^{-1} \text{ cm}^{-2}$ ). A possible extrapolation of the new  $\log N - \log P$  distribution to lower brightnesses would probably imply a much larger rate of up to several thousands of GRBs per year.

The best possible efficiency and scan quality have still not yet been achieved. When we repeated the scan for a fraction of data scanned early on, we found 13 new GRBs per 60 days. This means that an additional considerable increase of the statistics of the weakest GRBs is possible (as is an extension of the statistics of the weakest test bursts). There are obvious possibilities for improving the test burst method as was discussed in §2 and in Stern et al. (2000b), for improving the approximation of the background, etc. This means that a new scan is desirable.

This research made use of data obtained through the HEASARC Online Service provided by NASA/GSFC. We are grateful to R. Preece who supplied us with valuable information and suggested one of the used tests for the sample contamination. We are grateful to J. Kommers who inspected a large part of our sample and thus helped us to eliminate non-GRB contamination. We thank A. Beloborodov for useful discussions. We thank A. Skassyrskaya, A. Skorbin, E. Stern, V. Kurt, K. Semenkov, S. Masolkin, A. Sergeev, M. Voronkov, and F. Ryde for assistance. This work was supported by the Swedish Natural Science Research Council, the Royal Swedish Academy of Science, the Wennergren Foundation for Scientific Research, a NORDITA Nordic Collaboration Project grant, and the Swedish Institute. D. K. was supported by RFBR grant 97-02-16975.

## REFERENCES

Band, D., et al. 1993, ApJ, 413, 281  
 Fishman, G. J., et al. 1989, in Proc. of the Gamma Ray Observatory Science Workshop, ed. W. N. Johnson (Greenbelt: Goddard Space Flight Center), 3-47

Kommers, J. M., Lewin, W. H. G., Kouveliotou, C., van Paradijs, J., Pendleton, G. N., Meegan, C. A., & Fishman, G. J. 1997, ApJ, 491, 704 (K97)

Kommers, J. M., Lewin, W. H. G., Kouveliotou, C., van Paradijs, J., Pendleton, G. N., Meegan, C. A., & Fishman, G. J. 1998, Current Non-triggered Supplement to the BATSE Gamma-Ray Burst Catalog (MIT Center for Space Research) (K98)

Kommers, J. M. , Lewin, W. H. G., Kouveliotou, C., van Paradijs, J., Pendleton, G. N., Meegan, C. A., & Fishman, G. J. 2000, *ApJ*, 533, 696 (K00)

Kouveliotou, C., Meegan, C. A., Fishman, G. J., Bhat, N. P., Briggs, M. S., Koshut, T. M., Paciesas, W. S., & Pendleton, G. N. 1993, *ApJ*, 413, L101

Nemiroff, R.J., Norris, J.P., Bonnell, J.T., Wickramasinghe, W.A.D.T., Kouveliotou, C.; Paciesas, W.S., Fishman, G.J., & Meegan, C.A. 1994, *ApJ*, 435, L133

Paciesas, W. S., et al. 1999, *ApJS*, 122, 465

Pendleton, G. N., et al. 1999, *ApJ*, 512, 362

Rubin, B. C., Horack, J. M., Brock, M. N., Meegan, C. A., Fishman, G. J., Wilson, R. B., Paciesas, W. S., & van Paradijs, J. 1992, in AIP Conf Proc. 280, Compton Gamma Ray Observatory, ed. M. Friedlander, N. Gehrels, & D. J. Macomb (New York: AIP), 719

Schmidt, M. 1999, *A&AS*, 138, 409

Stern, B. E., Poutanen, J., & Svensson, R. 1999, *ApJ*, 510, 312

Stern, B. E., Tikhomirova, Ya., Stepanov, M., Kompaneets, D., Berezhnoy, A., & Svensson R. 1999a, *A&AS*, 138, 413

Stern, B. E., Tikhomirova, Ya., Kompaneets, D., Stepanov, M., Berezhnoy, A., & Svensson R. 1999b, in ASP Conf. Ser. 190, Gamma Ray Bursts: The First Three Minutes, ed. J. Poutanen, & R. Svensson (San Francisco: ASP), 253

Stern, B. E., & Tikhomirova, Ya. 1999, FTP-archive of Gamma-Ray Bursts Found in the Continuous Batse Daily Records (Saltsjöbaden: Stockholm Observatory)

Stern, B. E., Tikhomirova, Ya., Stepanov, M., Kompaneets, D., Berezhnoy, A., & Svensson, R. 2000a, in Proc. of the Fifth Huntsville Symposium on Gamma-Ray Bursts, ed. R. M. Kippen, R. S. Mallozzi, & V. Connaughton, (New York: AIP), in press

Stern B. E., Tikhomirova Ya, Stepanov M, Kompaneets D., Berezhnoy A., & Svensson R. 2000b, *ApJL*, 540, L21

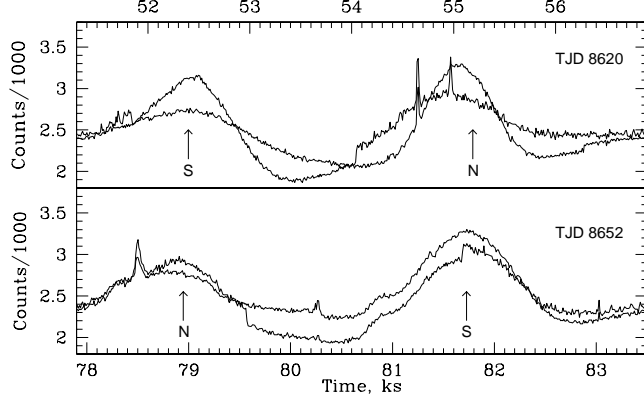


FIG. 1.— Two fragments of the daily data, each corresponding to one orbital period. Counts rates averaged over ten 1.024 bins are shown for 2 detectors in the 50 - 300 keV range. Features of the count rate curves are: (Upper panel) <51 800 s - strong noise from Cyg X-1 which is in its bright hard state; 51 800 s - descent of Cyg X-1; 52 400 s - *CGRO* reaches its most Southern latitude; 54 050 s - rise of Cyg X-1; 54 660 s - particle precipitation visible in all 8 detectors; 54 930 s - a solar flare; 55 200 s - *CGRO* reaches its most Northern latitude; 56 270 s - rise of the Crab nebula. (Lower panel) 78 500 s - particle precipitation; 79 550 s - descent of Cyg X-1; 80 250 s - a non-triggered GRB (the brightest and the third brightest detectors); 81 700 s - rise of Cyg X-1; 83 030 s - a non-triggered GRB (the two brightest detectors). This is a rare case of observing two non-triggered GRBs during one orbit. Both are very confident. They have peak fluxes of 0.14 and 0.21  $\text{ph s}^{-1} \text{cm}^{-2}$ , respectively.

TABLE 1  
PARAMETERS FOR THE 11 WEAKEST GRBS IN THE  
SAMPLE

Name	<i>c</i>	<i>I</i>	Sign.	$\delta_1$ (deg.)	$\delta_4$ (deg.)
08730a	0.049	0.072	17	18	37
08913c	0.049	0.088	11	23	43
09201c	0.045	0.076	15	33	70
09486b	0.045	0.076	14	24	47
09882b	0.047	0.077	9.1	33	61
10237b	0.047	0.081	10	39	84
10330a	0.045	0.072	8.5	37	67
10353d	0.038	0.066	16	20	41
10757a	0.047	0.081	7.6	24	75
10798a	0.044	0.075	9.5	39	84
10856d	0.038	0.088	14	44	60

Note. — Name is TJD of event plus an identifying letter; *c* is peak count rate in units of  $\text{counts s}^{-1} \text{cm}^{-2}$ ; *I* is peak flux in units of  $\text{photons s}^{-1} \text{cm}^{-2}$ ; significance is estimated using the residual  $\chi^2$  relative to the linear background in units of  $\sigma = \sqrt{2N}$  where *N* is the number of the degrees of freedom;  $\delta_1$  and  $\delta_4$  are defined in §4.

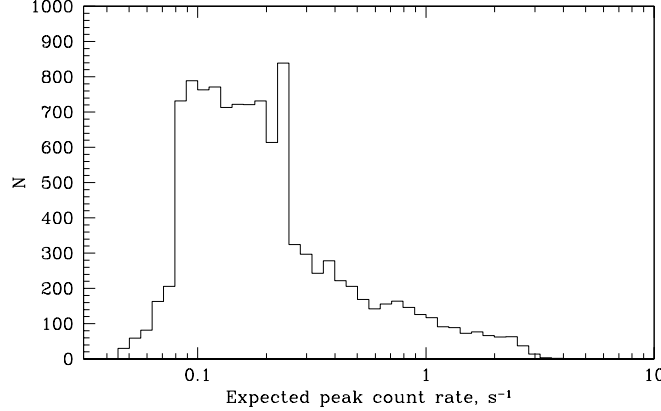


FIG. 2.— The peak count rate distribution of test bursts added to the data (for transformation of these units to photons  $\text{s}^{-1} \text{cm}^{-2}$  or to total counts, see § 5.2). Test bursts are included here independently of whether they were detected or missed. The BATSE threshold is around 0.15 counts  $\text{s}^{-1} \text{cm}^{-2}$ . The strange shape of the distribution resulted from changes in the sampling scheme during the scan.

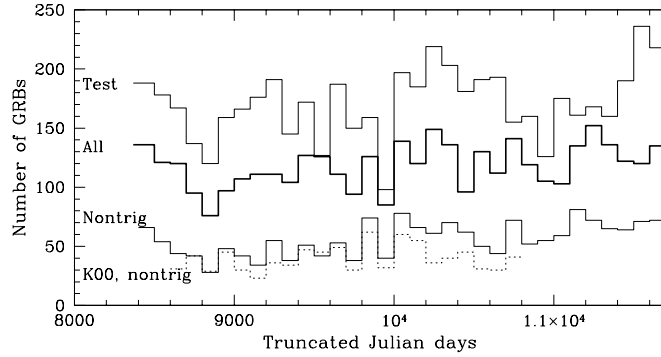


FIG. 3.— Time history of the rate of GRB detections during the scan for (from top to bottom) test bursts, all real bursts, non-triggered bursts, and non-triggered bursts of K98. The two deepest minima at TJD 8800-8900 and 9900-10000 and are caused by bright X-ray novae.

TABLE 2  
THE “LOW BRIGHTNESS” PART OF THE EFFICIENCY MATRIX

$\log c_m$	$\log c_e$						
	-1.3	-1.2	-1.1	-1.0	-0.9	-0.8	-0.7
-0.7	0.000	0.000	0.000	0.000	0.007	0.117	<b>0.431</b>
-0.8	0.000	0.000	0.003	0.010	0.121	<b>0.365</b>	0.110
-0.9	0.000	0.000	0.018	0.104	<b>0.286</b>	0.112	0.007
-1.0	0.000	0.008	0.068	<b>0.159</b>	0.095	0.013	0.004
-1.1	0.000	0.043	<b>0.069</b>	0.065	0.010	0.001	0.000
-1.2	0.000	<b>0.004</b>	0.029	0.008	0.002	0.001	0.001
-1.3	<b>0.000</b>	0.012	0.000	0.000	0.000	0.000	0.000

Note. — The Table shows the probability,  $F(c_e, c_m)$ , for the detection of a GRB with an expected peak count  $c_e$  and a measured peak count rate  $c_m$ . The vertical and horizontal bins are uniform in the logarithm of  $c$ . The lower edges of the bins are given in terms of  $\log(c_{e,m})$ . Units are counts  $\text{s}^{-1} \text{cm}^{-2}$ .

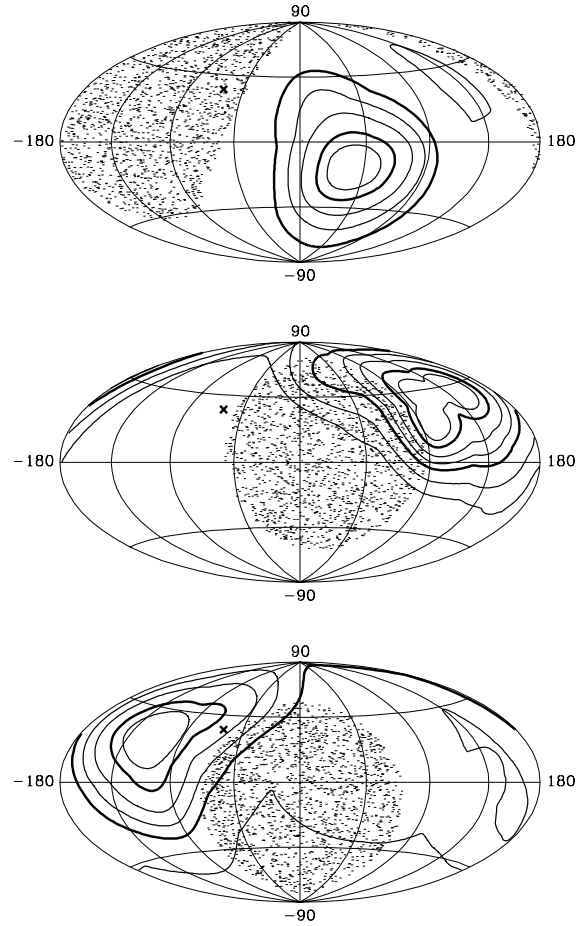


FIG. 4.— Residual  $\chi^2$  maps of the sky for three weak events (09394b, 09575a, and 09590c, where the name consists of TJD and an identifying letter), which passed the selection criteria being near the  $\delta_4$  threshold (see text) of the significance. These events were chosen among the least reliable cases. The time profiles for these events are shown in Figure 5. Isocontours show constant levels of the residual  $\chi^2$  measured as  $(\chi^2 - \chi_0^2)/\sigma$  where  $\chi_0^2$  is the minimum,  $\sigma = \sqrt{2N}$  where  $N$  is the number of the degrees of freedom. The levels of  $0.5\sigma$ ,  $1\sigma$  (bold contour),  $2\sigma$ ,  $3\sigma$ ,  $4\sigma$  (bold contour),  $6\sigma$ , and  $8\sigma$  are shown. The dashed area represents the Earth. The cross shows the location of Cyg X-1.

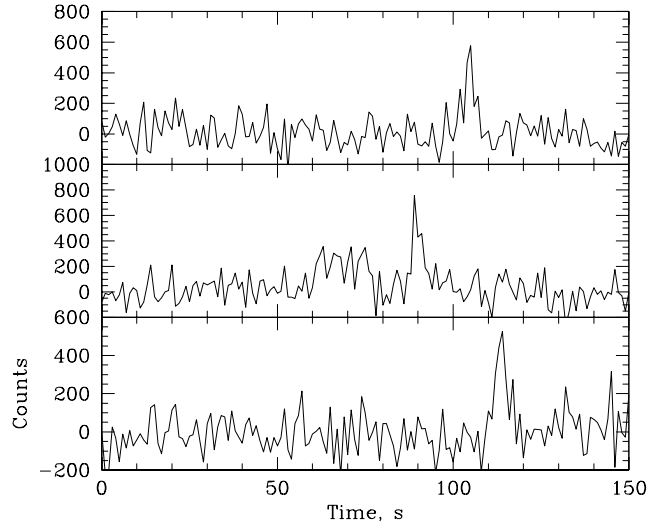


FIG. 5.— Count rate time profiles for the 3 events that are shown in Figure 4.

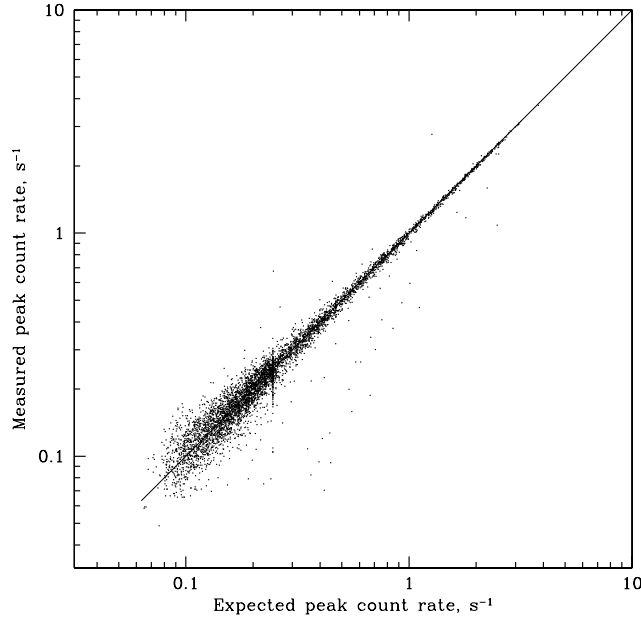


FIG. 6.— Measured vs expected peak count rates for detected test bursts. Several points having a measured count rate much lower than expected are affected by data gaps causing the peak of the event to be lost. Two points, where the measured count rate is much higher, are probably due to confusion of the test burst with an overlapping brighter real event.

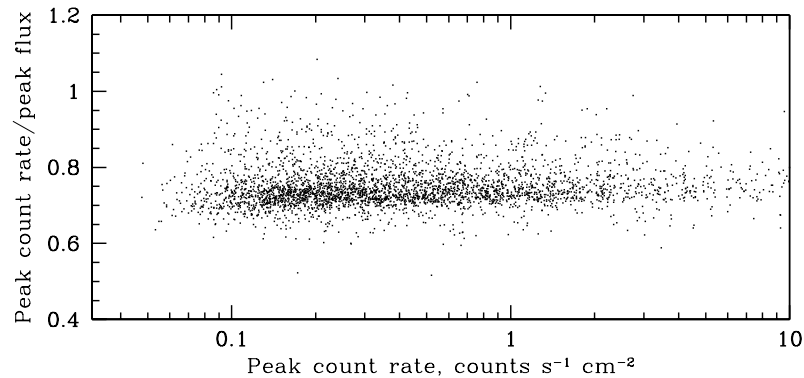


FIG. 7.— Peak count rate measured in counts  $s^{-1} cm^{-2}$  (channels 2+3) versus the peak flux in the 50 - 300 keV band measured in photons  $s^{-1} cm^{-2}$ . A few events with  $c/I > 1$  are due to strong atmospheric scattering and to the hard part of the spectra contributing to channels 2 and 3 due to Compton scattering in the detectors.

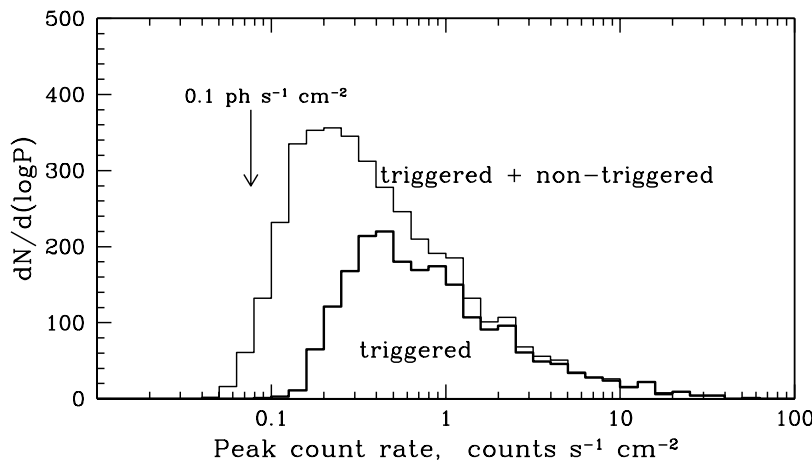


FIG. 8.— Peak count rate distribution,  $dN/d(\log P)$ , of the 2074 BATSE-triggered GRBs detected in our scan (thick histogram) and of all 3923 GRBs detected in our scan (thin histogram). The distributions have not been corrected for the efficiency.

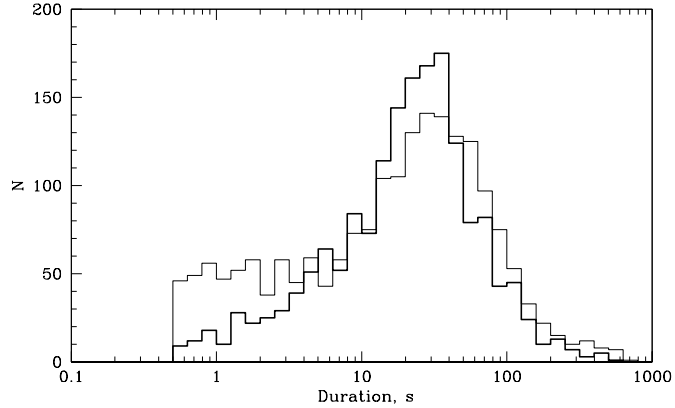


FIG. 9.— Duration distribution ( $T_{90}$ ) for 1965 triggered (thick line histogram) and 1713 nontriggered (thin line histogram) bursts detected up to TJD 11499. For clarity, the discreteness of the distribution was smoothed by a uniform random distribution of  $T_{90}$  for an  $n^{\text{th}}$ -bin event into the interval  $(n-1)1.024 \text{ s} < T_{90} < n1.024 \text{ s}$  for  $n > 1$  and into the interval  $0.5 \text{ s} < T_{90} < 1.024 \text{ s}$  for  $n = 1$ . The distribution at  $T_{90} < 4 \text{ s}$  is biased (see text and Fig. 10).

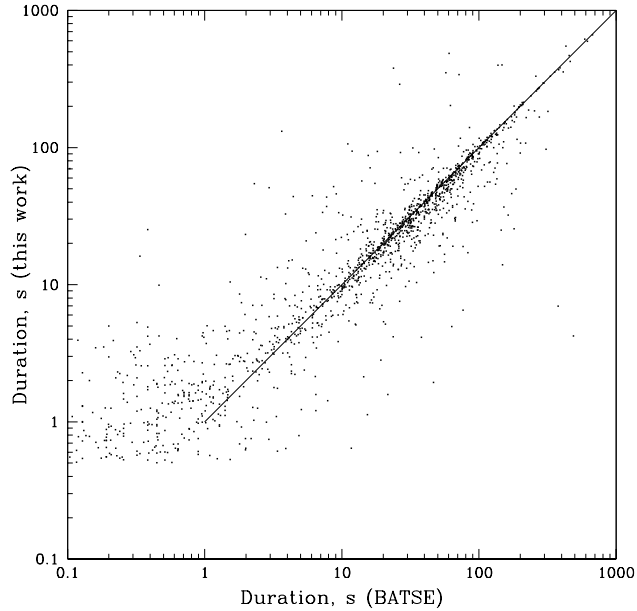


FIG. 10.— Comparison between BATSE and our estimates of  $T_{90}$  for the 1965 bursts detected both by BATSE and by us up to TJD 11499. For clarity, our estimates are dispersed as described in Figure 9.

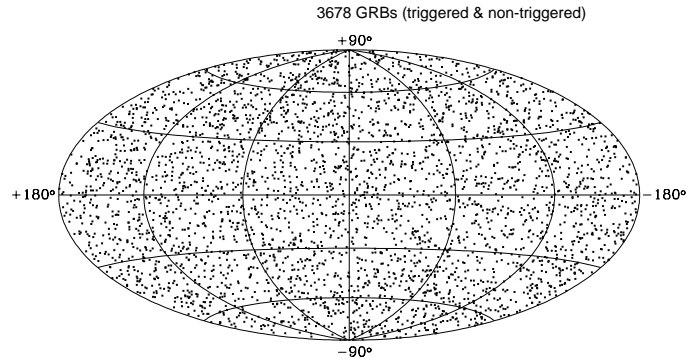


FIG. 11.— Map of best fit locations of our GRBs detected up to TJD 11499 in galactic coordinates.

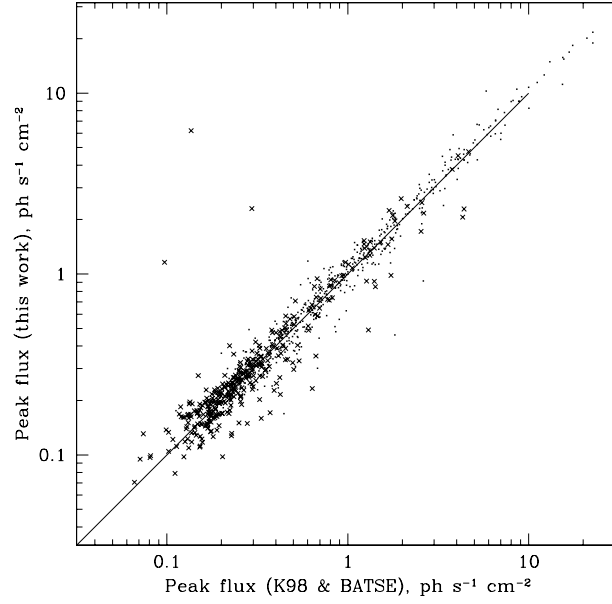


FIG. 12.— Our estimates of the peak flux in the 50 - 300 keV range versus the K98 estimates for the same non-triggered bursts (crosses) and the BATSE estimates for triggered bursts (dots) in 1.024 s time resolution. For clarity, only  $\sim 30\%$  of the sample is shown.

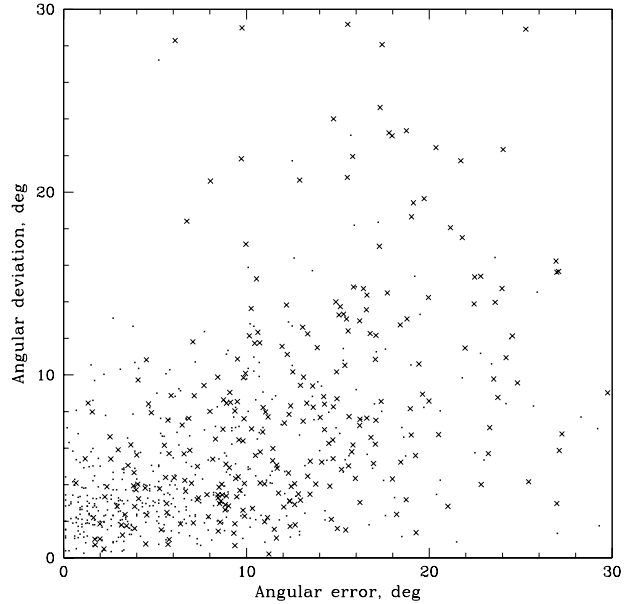


FIG. 13.— Angular deviations between our and the K98 best fit locations (crosses) and between our and the BATSE locations (dots) versus the  $1\sigma$  localization errors according to our estimates. For clarity, only  $\sim 30\%$  of the sample is shown.

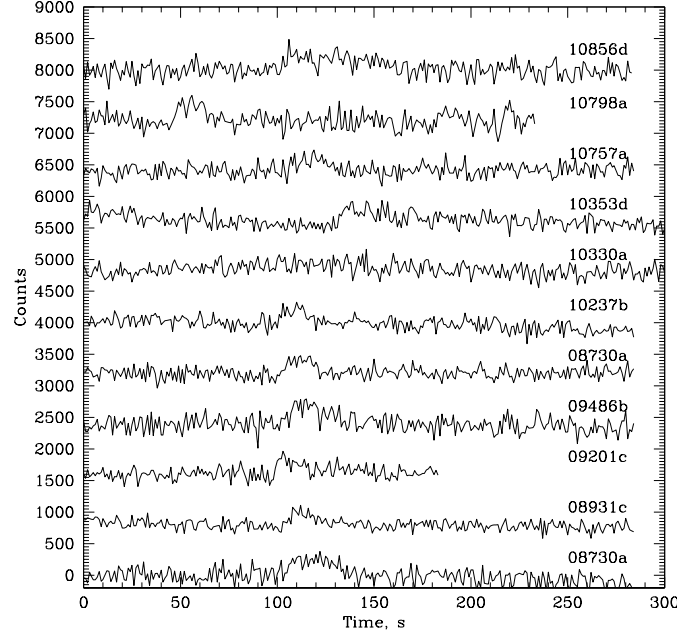


FIG. 14.— Fitting count rate time profiles for the eleven weakest events detected in our scan. The event 10330a can hardly be recognized on this scale due to its long duration ( $\sim 150$  s) and smoothness. Nevertheless, this is a confident event clearly visible on a longer time scale and at a wider time binning. The time profiles have been shifted vertically for clarity.

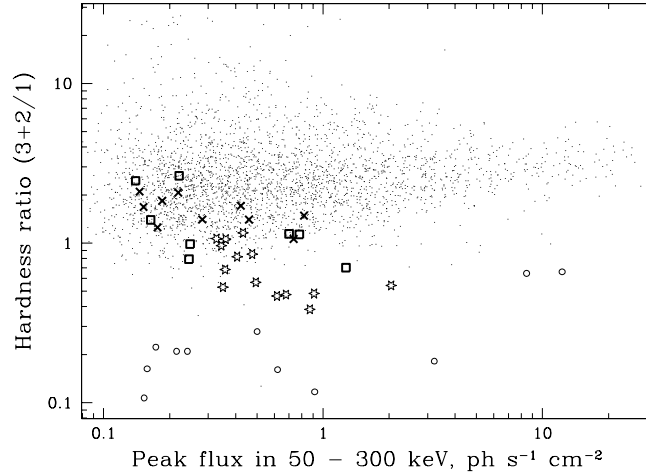


FIG. 15.— Hardness ratio (the integral of the counts in channels 2 and 3, 50 - 300 keV, to that in channel 1, 20 - 50 keV) for GRBs (dots) and for different kinds of non-GRB events. Crosses: Cyg X-1; squares: ionospheric phenomena; stars: X-ray pulsars (two objects), circles: solar flares.

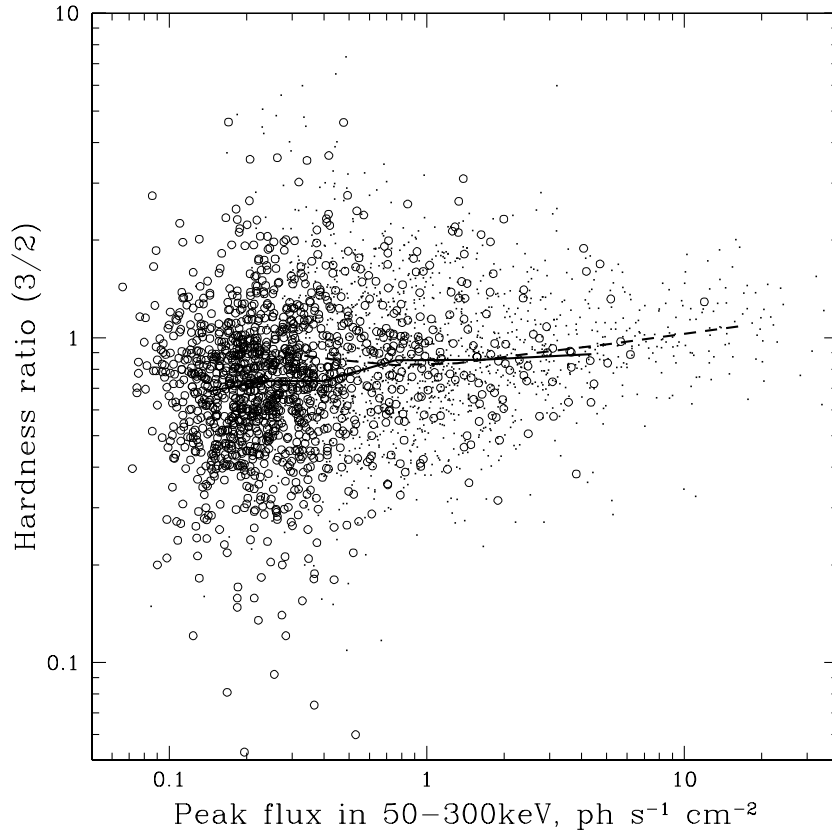


FIG. 16.— Hardness versus the 50-300 keV peak flux for the GRBs detected in the scan. The hardness ratio is here the ratio of the time-integrated peak count rate in the BATSE LAD channel #3 (100 - 300 keV) to that in channel #2 (50 - 100 keV). Solid curve shows the median hardness ratio for triggered GRBs, while the dashed curve shows the same for non-triggered GRBs. Circles represent the 1849 non-triggered GRBs, while dots represent the 2074 BATSE-triggered GRBs detected in the scan. Weak triggered GRBs are harder than non-triggered ones in the same peak flux range because of short hard events which are weak at 1024 ms resolution but which are easily triggered at 64 ms resolution. The general trends approximately agrees with the results of Nemiroff et al. (1994).

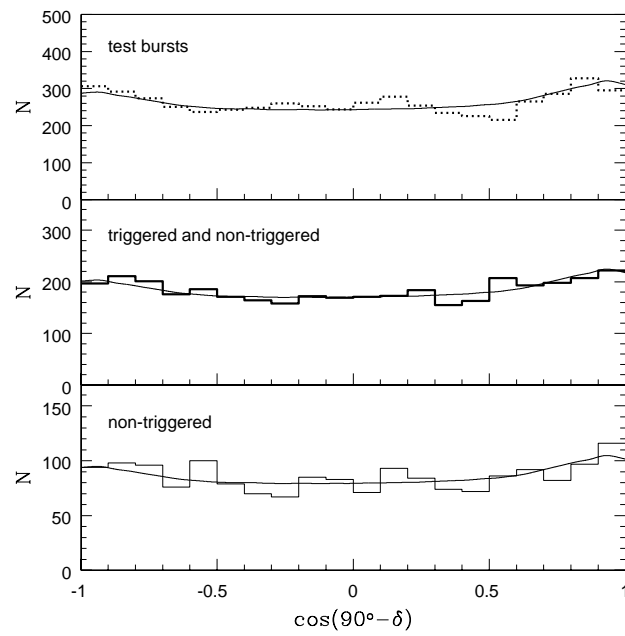


FIG. 17.— Polar annular distributions of GRBs and test bursts. Smooth curves show the BATSE exposure function.

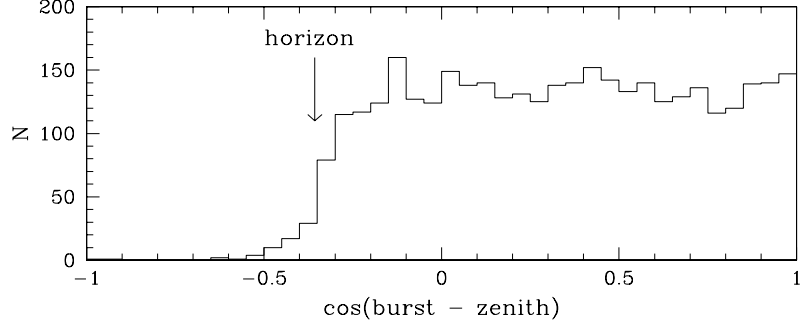


FIG. 18.— The distribution of GRBs locations in coordinates associated with the Earth. The position of the Earth's horizon is shown by the arrow.

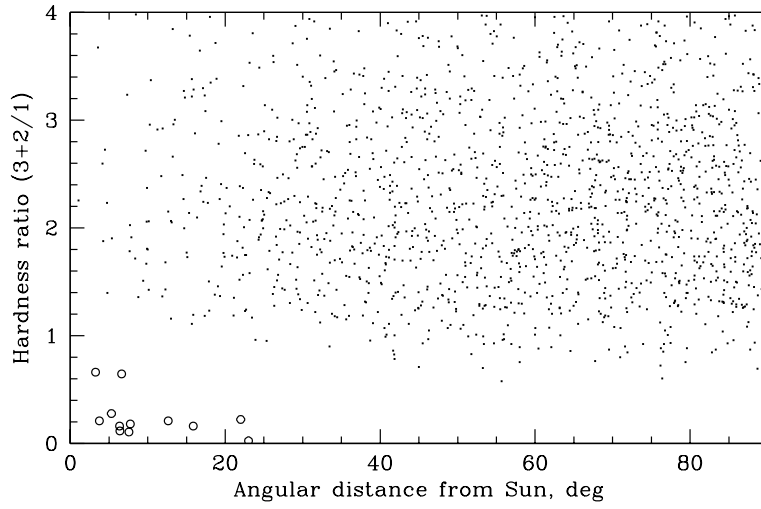


FIG. 19.— Hardness ratio vs. angular separation from the Sun for GRBs (dots) and several solar flares (circles).

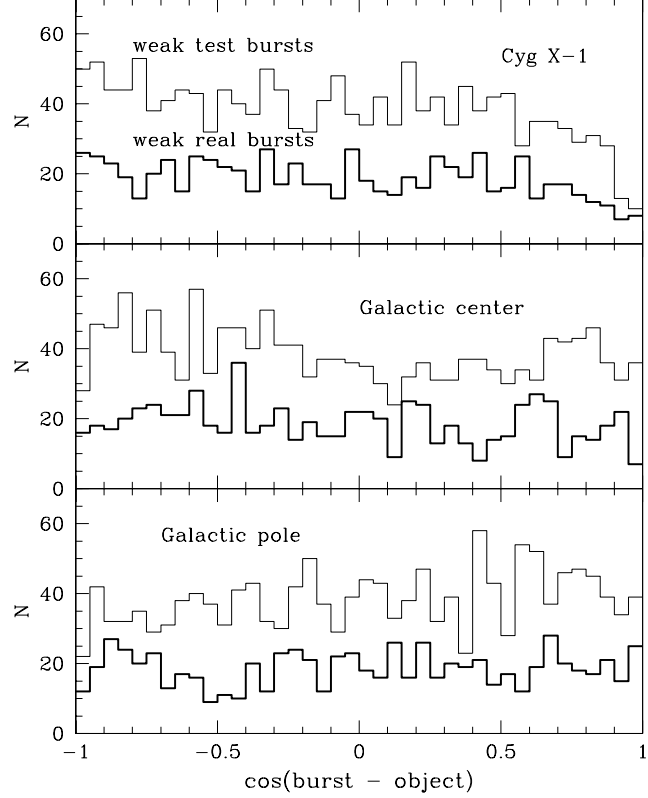


FIG. 20.— Angular distributions of detected bursts in different coordinate systems.

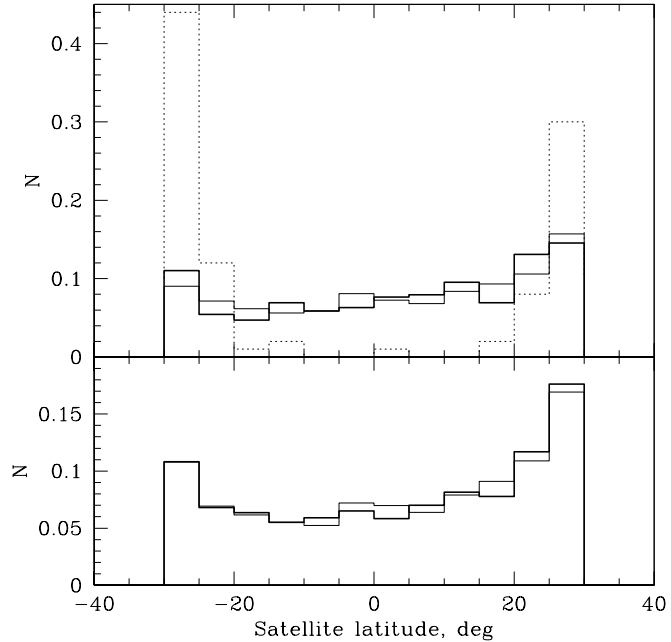


FIG. 21.— Distributions of detected bursts and particle precipitation events over the latitude of *CGRO* at the time of detection. Upper panel: weak events (peak flux  $< 0.2 \text{ ph s}^{-1} \text{ cm}^{-2}$ ); lower panel: all events. Thick line histograms: real bursts; thin line histograms: test bursts; dotted line histogram: a sample of 100 particle precipitation events detected during different time intervals of observations. The asymmetric shape of the burst histograms is mainly due to the effect of the South Atlantic magnetic anomaly where any detection is impossible because of a very large ionospheric background.

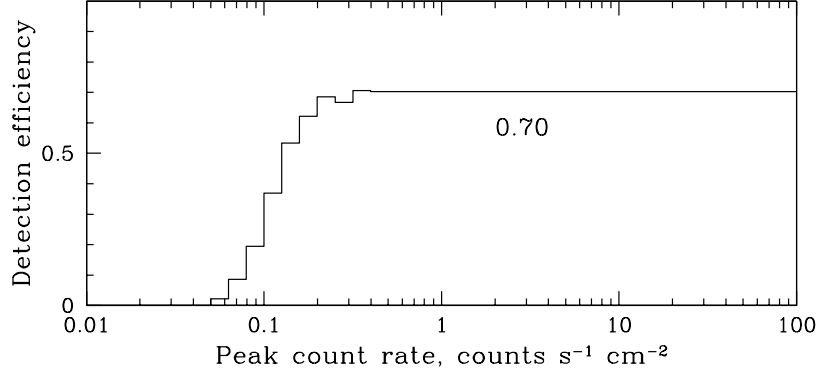


FIG. 22.— The efficiency of the off-line burst detection defined as the fraction of the test bursts detected in our scan versus the peak count rate,  $P$ . The efficiency is normalized to the total number of events occurring above the Earth's horizon.

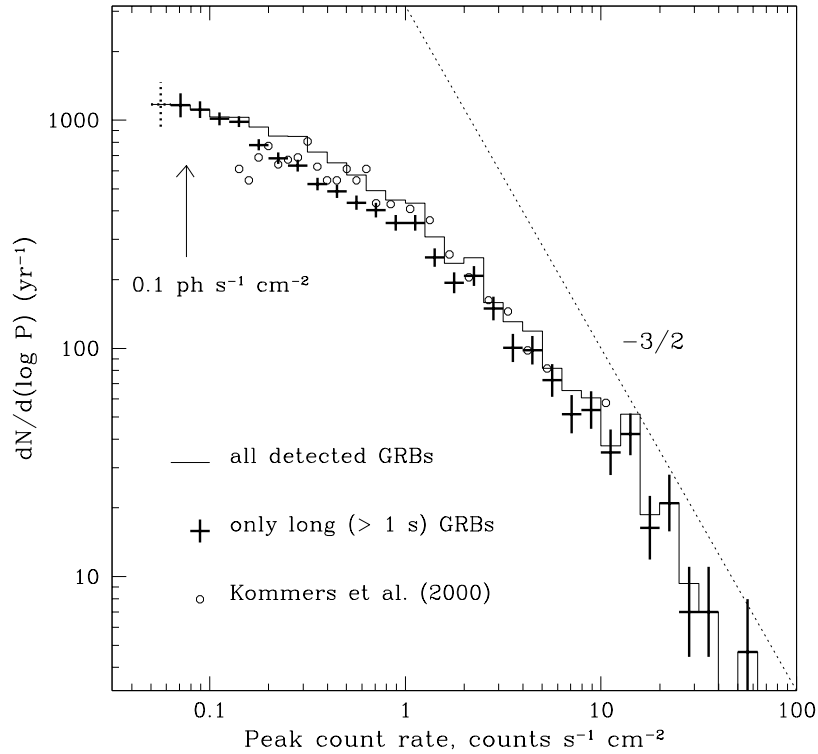


FIG. 23.— The differential  $\log N - \log P$  distribution corrected for the efficiency function in absolute units for all 3923 GRBs detected in our scan (histogram) and for the 3300 events in our sample with a duration longer than 1 s (crosses). The corresponding distribution in absolute units for the 2265 GRBs (of any duration) found by K00 is shown by circles (the K00 data were transformed to count rates by applying the factor 0.75, see §5.2 and Figure 7). The leftmost dashed data point is probably affected by the threshold bias arising from errors in the peak count rates.